Experimental observation and investigation of energy exchange between an electron beam and counterpropagating laser beams in a Compton-scattering free-electron-laser scheme

R. Z. Olshan, A. Gover, S. Ruschin, H. Kleinman, and A. Friedman
Department of Electron Devices, Faculty of Engineering, Tel-Aviv University, Tel-Aviv, Israel
(Received 29 January 1988)

We report the observation and investigation of synchronous energy exchange between nonrelativistic electrons and the ponderomotive (beat) force of two counterpropagating intense pulsed CO_2 laser beams, operating at different frequencies in a stimulated Compton-scattering scheme. The interaction occurred in the nonlinear (trapping) regime, the physics of which is the same as that which occurs in laser accelerators and efficiency-enhanced free-electron lasers (FEL's) with long wigglers. The experiment is a first demonstration of the principle of inverse FEL acceleration and electromagnetic pump FEL operation in the nonlinear (trapping) regime. It can also be described as a demonstration of a "traveling beat-wave" Kapitza-Dirac effect in the nonlinear regime. Two different mechanisms of enhanced energy transfer were observed—electron trapping and phase-area displacement. Experimental results and computer simulations of both mechanisms are presented.

I. INTRODUCTION

This paper describes the theory, simulations, and experimental results of an ongoing experiment in which energy transfer between a nonrelativistic electron beam and the traveling beat wave of two counterpropagating CO_2 laser beams was distinctly observed.[1] The experiment serves to investigate nonlinear-regime stimulated Compton scattering in an electromagnetic wiggler free-electron laser (FEL) scheme, as well as inverse FEL (laser accelerator) schemes.

A single electron cannot exchange energy with a single photon in free space because conservation of both energy and momentum conditions cannot be satisfied simultaneously. Consequently, the lowest-order radiative interaction process in free space involves two photons. The most basic process of this kind is Compton scattering.

A *stimulated* Compton scattering effect was predicted in 1933 by Kapitza and Dirac.[2] In their configuration two counterpropagating electromagnetic (em) waves of equal frequency form a standing wave. If an electron, propagating transversely to the waves, scatters a photon from one traveling wave to the other, it obtains transverse momentum $2\hbar\omega/c$, and therefore may be deflected by an angle of $(2\hbar\omega/c)/(\gamma mv)$. As the em wave intensities are increased, the deflection process can be described as electron diffraction by a spatially periodic ponderomotive potential "grating," which is generated by the beat of the two em waves.[3]

If the free electron is propagating in a counter direction to an incoming em wave, the scattered Compton radiation exhibits a Doppler shift. In the case of backscattering, the scattered (signal) wave frequency ω_s is related to the incoming (wiggler) wave frequency ω_w by

$$\frac{\omega_s}{\omega_w}=\frac{1+\beta_z}{1-\beta_z}\ , \tag{1}$$

where $\beta_z=v_z/c$ is the electron axial velocity, and the small-quantum-recoil effect was neglected. At relativistic electron velocities the Doppler shift associated with (1) may be appreciable, and this can be utilized to advantage in stimulated Compton-scattering FEL, where the signal wave is amplified by the stimulated Compton scattering process.[4] Similar stimulated emission or absorption may also be obtained with a periodic magnetostatic wiggler field, as employed in magnetic bremsstrahlung FEL's[5] and laser accelerators.[6]

In order to observe an appreciable interaction effect between the electrons and the traveling beat wave, the electron velocity must be synchronized with the beat-wave phase velocity $v_r=(\omega_s-\omega_w)/(k_s+k_w)$ (for a static wiggler $\omega_w=0$). The relative velocity between the electron and the wave can be scanned by applying an axial E field. In the nonlinear regime, where deep ponderomotive potential wells (traps) form, two different physical situations may occur: (1) Electrons inserted into the interaction region are within the phase-space area of initially synchronous traps [trapping—see Figs. 1(a) and 1(c)], and (2) the opposite case of no initial trapping [Figs. 1(b) and 1(d)]. If the axial E field and other interaction parameters are uniform along the entire interaction length, the initially trapped electrons occupy closed trajectories inside the trap area, and remain trapped despite the accelerating field. In both cases the initially untrapped electrons accelerate or decelerate freely, following open phase-space trajectories. Transitions between trapped and untrapped electron trajectories are possible only if the interaction parameters are changed nonadiabatically in either the axial or time dimension, or if the electron is displaced transversely across the optical beams.

The phase-space diagram of Fig. 1(a) depicts partial initial trapping in a tapered wiggler FEL efficiency-enhancement scheme. As the electrons lose energy by radiating into the signal field, their velocity decreases, and the radiative process becomes saturated. The tapering of the wiggler period induces the trapped electrons to continue to radiate past the saturation point of a linear wiggler.[7] The analogous trapped electron-efficiency-enhancement scheme with an applied axial E field is illus-

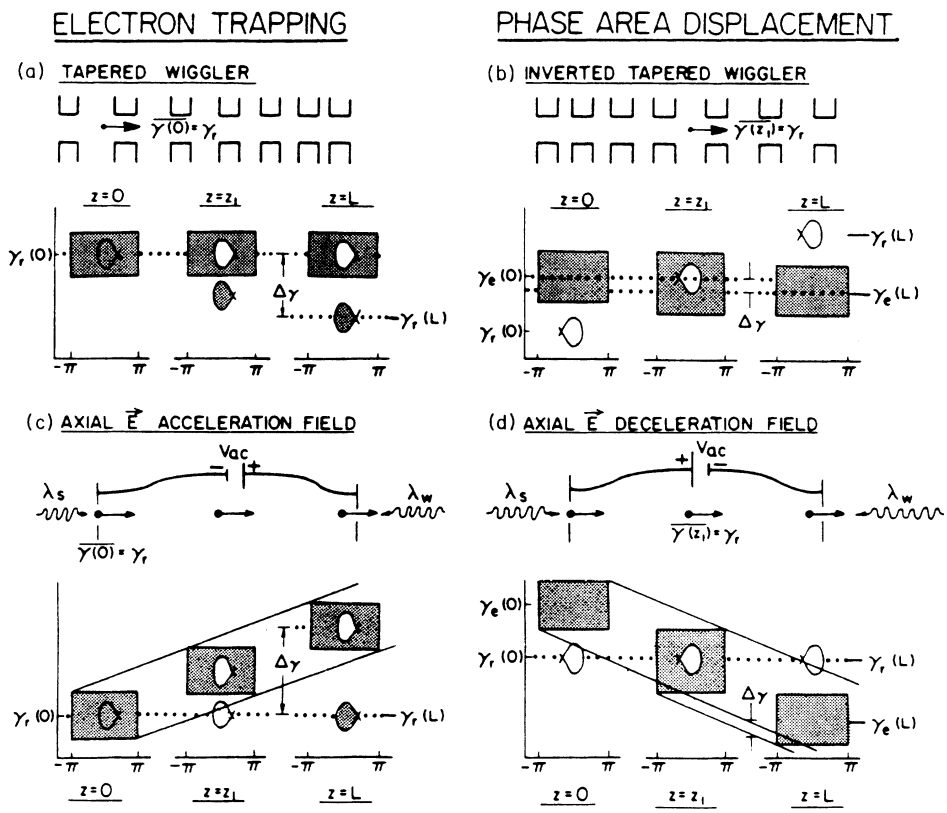

FIG. 1. Phase-space diagrams for electron energy extraction: (a) and (c) electron trapping; (b) and (d) phase-area displacement.

trated in the phase-space diagram of Fig. 1(b). Electrons initially trapped by a constant velocity ponderomotive potential wave must remain trapped and therefore are not accelerated. Consequently, the energy invested by the external axial field induces the electrons to produce enhanced stimulated Compton-scattering radiation into the signal field.

An additional mechanism of radiative energy extraction termed "phase-area displacement"[7,8] (PAD), results in enhanced signal amplification when the entire e beam is scanned through the synchronism condition, as depicted in Figs. 1(c) and 1(d). In PAD as opposed to electron trapping, signal amplification is accomplished by either reversing the taper in a tapered wiggler, or by reversing the polarity of the dc field. In both PAD schemes, trapping conditions at the entrance to the interaction region are avoided, and all the electrons are scanned through the energy of synchronism at some point along the interaction region, resulting in a net energy extraction from the entire electron beam. Note that for axial field acceleration with the same polarity dc field, the trapped electron and the PAD mechanisms would result in energy exchange with the radiation fields in opposite directions.

The FEL efficiency-enchancement scheme of a tapered-period static wiggler with a decelerating beat wave [Fig. 1(a)] has essentially the same physics as the axial acceleration E-field scheme[9] [Fig. 1(c)]. Tapered wiggler FEL's were recently demonstrated to operate with remarkable efficiencies.[10] Laser accelerators with inverse tapering [Fig. 1(b)] have been considered,[6] and PAD FEL schemes [Fig. 1(d)] have been proposed,[7,8] but neither have yet been tried. An alternative experimental tool for studying electron interactions with intense radiation fields aside from static wiggler FEL's is the stimulated Compton-scattering scheme and has not until now been exploited. Current state of the art high-intensity lasers make it possible to study these interaction effects in both the linear and nonlinear regimes. There have been investigations of stimulated Compton scattering in the Kapitza-Dirac configuration[11] which utilized the high-intensity standing-wave field inside the cavity of a Ruby laser.

II. THEORETICAL BASIS

The basic theory of electron trapping and PAD efficiency-enhancement schemes in magnetic bremsstrahlung FEL's is given in Refs. 7 and 8. The electron axial motion is governed by the longitudinal force equation

$$\frac{d(\gamma m v_z)}{dt} = -eE_{\rm ac} - eE_p \cos[\psi(z,t)] , \tag{2}$$

where $E_{\rm ac}$ is an externally applied axial accelerating or decelerating dc electric field, and E_p is the ponderomotive field amplitude, which for the case of an em wiggler is given by[12]

$$E_p = \frac{e\sqrt{\mu_0/\epsilon_0}}{\gamma_r mc^2}(\lambda_s+\lambda_w)\,|\,\hat{\mathbf{e}}_s\cdot\hat{\mathbf{e}}_w^*\,|\,\frac{\sqrt{P_w P_s}}{\pi w_{os} w_{ow}} , \tag{3}$$

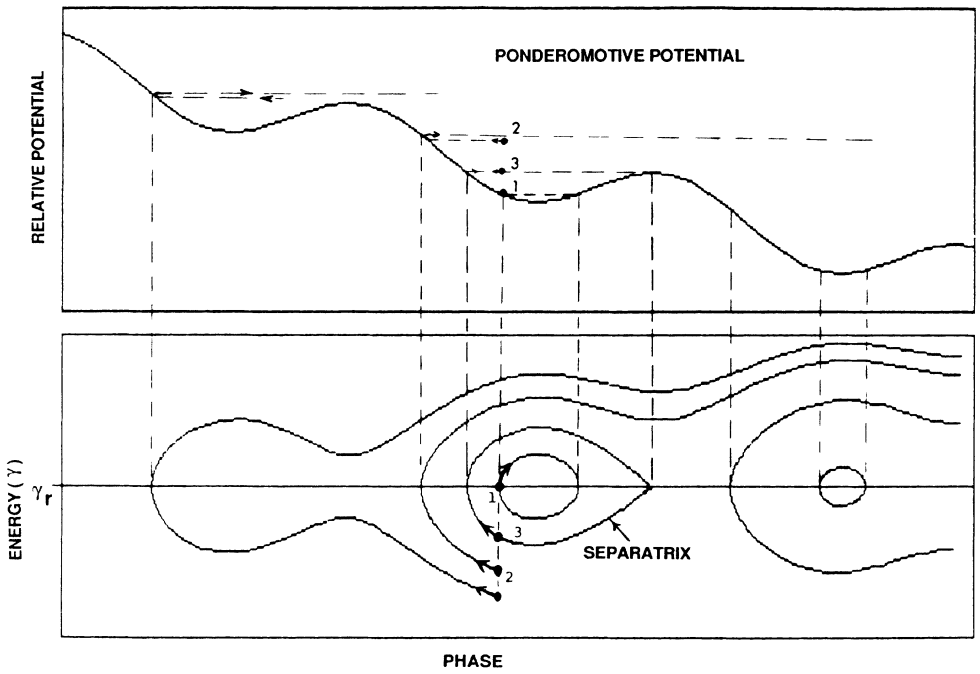

FIG. 2. Ponderomotive potential and electron energy and phase trajectories.

where $\hat{\mathbf{e}}_i$, P_i, w_{oi} $(i=w,s)$ are the polarization unit vectors, the powers and beam waists of the wiggler and signal waves, respectively. The phase of the electron relative to the ponderomotive wave is $\psi=(\omega_s-\omega_w)t-(k_s+k_w)z$.

First integration of the pendulumlike equation results in closed- (trapped) or open-electron phase-space orbits. A few electron energy and phase paths are plotted along with the ponderomotive potential in Fig. 2. The energy plotted is the normalized energy deviation from resonance and is given by

$$\delta\gamma=\pm\{(\delta\gamma_{\max})^2+(\delta\gamma_t^0)^2[\cos\psi+(\psi-\psi_r)\sin\psi_r-\cos\psi_r]/2\}^{1/2}, \tag{4}$$

where ψ_r is the electron phase at resonance with the ponderomotive wave and is given by

$$\psi_r=\arcsin\left[\frac{E_{\rm ac}}{E_{\rm p}}\right]. \tag{5}$$

$\delta\gamma_{\max}$ is a parameter that characterizes the orbit and corresponds to the maximum for closed orbits. The largest of the closed-electron trajectories is defined as the separatrix (depicted as path number 3 in Fig. 2) and is given by

$$\delta\gamma_{\rm sep}(\psi)=\pm(\delta\gamma_t^0)\{[\cos\psi_r+(\psi+\psi_r-\pi)\sin\psi_r+\cos\psi]/2\}^{1/2}. \tag{6}$$

The separatrix function is characterized by two parameters, as indicated in Fig. 3, the resonant phase ψ_r, and the zero-field half width of the trap $\delta\gamma_t^0$ which is given by[12]

$$\delta\gamma_t^0=\left[\frac{4e\beta^2\gamma^3E_p}{(k_s+k_w)mc^2}\right]^{1/2}. \tag{7}$$

For $\delta\gamma_{\max}<\delta\gamma_t^0$, the trajectories are closed (trapped electrons), and for $\delta\gamma_{\max}>\delta\gamma_t^0$ the trajectories are open. For $\psi_r=0$, the separatrix function reduces to $\delta\gamma=\delta\gamma_t^0|\cos(\psi/2)|$. For uniform acceleration along the interaction region, electrons trapped at the entrance to the interaction region remain trapped to the end [Fig. 1(c)]. Thus, the untrapped electrons are displaced by average energy $\Delta\bar{\gamma}$, relative to the trapped ones;

$$\Delta\bar{\gamma}=\frac{eE_{\rm ac}L}{mc^2}, \tag{8}$$

where L is the interaction length. For a warm electron beam $\Delta\gamma_{\rm th}\gg2\delta\gamma_{\max}$, the trapping efficiency will be $A_t/(2\pi\Delta\gamma_{\rm th})$, where A_t is the trap area ($A_t\simeq8\delta\gamma_t^0$ for $\psi_r\ll1$).

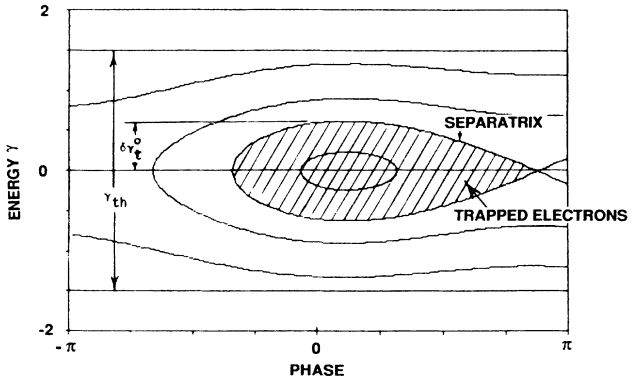

FIG. 3. Electron energy and phase trajectories.

If the decelerated or accelerated e beam synchronizes with the beat wave within (as opposed to at the start of) the interaction region [Figs. 1(b) and 1(d)], the beam will exchange average energy $\Delta\bar{\gamma}$ with the radiation field by the PAD mechanism. $\Delta\bar{\gamma}$ may be calculated by integration along phase-space paths of the electrons. For $\psi_r \ll 1$, neglecting edge effects, an approximate expression is derived[7,8]

$$\Delta\bar{\gamma} = \frac{A_t}{2\pi} = \frac{4\delta\gamma_t^0}{\pi} . \tag{9}$$

For an initial e-beam energy spread larger than the trap width, the average energy transfer will affect all the electrons since all of the electrons pass through synchronism with the beat wave.

III. THE EXPERIMENTAL SCHEME

The experiment concept, as depicted in Fig. 4 with the baseline parameters listed in Table I, was described in detail by Olshan *et al.*[13] Two transversely excited atmospheric (TEA) CO_2 lasers produced the 9.3-μm signal wave and the 10.6-μm wiggler wave, both of which were operated in single longitudinal and transverse cavity modes. Their 100-nsec duration pulses were synchronized to arrive simultaneously at the interaction region during the 10-μsec pulse of the electron beam. The $\sim$1-keV electron-beam voltage was matched to the synchronism condition at either the entrance to the interaction region for setting trapping conditions [Figs. 1(a) and 1(c)] or within the interaction region for PAD conditions [Figs. 1(b) and 1(d)]. The e-beam energy spread was $\Delta E_{\text{th}} \simeq 4$ eV, with a grid-controlled current of 10–50 μA.

An axial electric force was exerted along the interaction length by employing the ohmic potential drop along a copper coil when a 1-msec, 500-A current pulse is applied to it. Accelerating or decelerating fields were achieved by changing the direction of the current. The coil current also provided an axial magnetic field which bent the e beam and guided it along the interaction region. The timing diagram of the three nested levels of pulses in the experiment are depicted in Fig. 5.

Both retarding-potential and time-of-flight electron-energy-analysis techniques were employed for diagnosing the electron-radiation interaction effects. In the first method a retarding potential electrode is placed in front of a Faraday cup collector and is biased to set partial e-beam reflection conditions ($V_{\text{ret}} = 0-7$ V). In the case of positive transfer of energy, some electrons (which in the absence of the radiation field would be reflected back to the cathode), gain enough energy in the radiative interaction to surpass the retarding potential barrier in front of the collector, and thereby form a pulse of excess electron current that arrives at the collector following the lasers pulse period. In the case of negative-energy transfer, a current deficient pulse would be measured. This deficiency is attributed to electrons which in the absence of a radiation field would be collected by the anode, but due to loss of energy in the radiative interaction during the onset of the laser beams, cannot surpass the retarding potential barrier preceeding the collector. In the time-of-flight technique, a metallic tube was inserted into the glass tube concentric with the copper coil in the straight section following the interaction region, as shown in Fig. 4. The metallic tube shields the electrons from the high

TABLE I. Experiment parameters.

Signal power	0.25 MW
Wiggler power	0.25 MW
Signal wavelength	9.261 μm
Wiggler wavelength	10.59 μm
Optical-beam waists (w_0)	1.77 mm
Coil current	0.5 KA
Energy spread (FWHM)	3 eV
Interaction length	0.6 m
Electron current	10 μA
Electron velocity	2.0×10^7 m/sec
Axial electric field	65 V/m
Resonance energy	1.153 KeV
Ponderomotive field	369.7 V/m
Trap depth	1.409 eV
Resonant phase ψ_r	0.2 rad

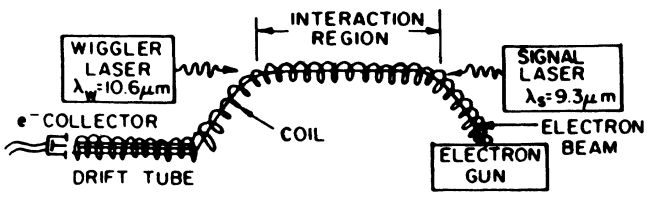

FIG. 4. Experiment concept.

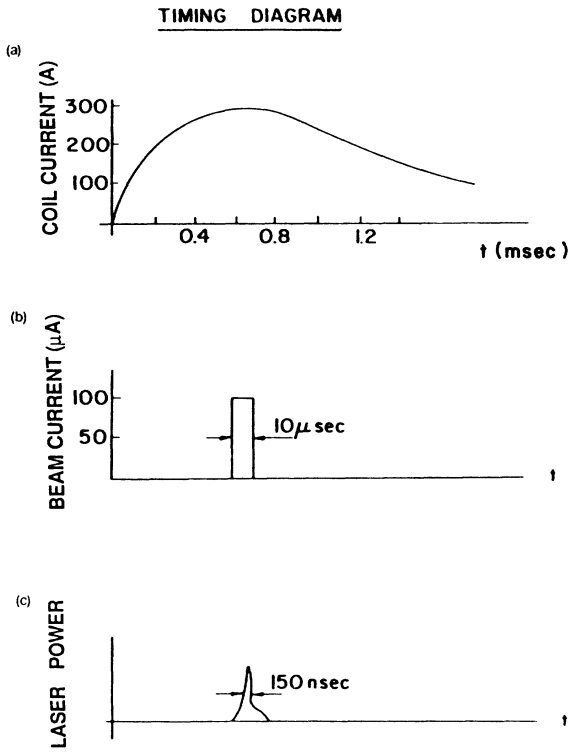

FIG. 5. Pulse timing diagram.

voltage of the coil and external electromagnetic noise. Hence the electrons may drift freely along its axis in a constant-potential field-free environment. The tube is biased to a low drift-tube voltage ($V_{DT}=10$ V) causing electrons of different velocities and corresponding different drift times to produce a time-dispersed current pulse which folds into it the electron energy spectrum after the interaction.

The electron current pulse and the laser pulses were recorded by three separate channels of high-speed digital transient recorders. The data was stored by an on-line computer for subsequent reduction, analysis, and interpretation.

To assure conditions of electron interaction with a pure traveling beat wave, both CO_2 lasers had to be operated in single longitudinal and transverse modes. This was achieved by different methods for the 10.6-μm and 9.3-μm lasers. The 9.3-μm single mode was attained by replacing the highly reflective mirror of a Lumonics TEA laser with a Fox-Smith interferometer, as illustrated in Fig. 6. The interferometer serves to internally suppress the undesired cavity resonances, hence permitting laser oscillation at only one frequency. We employed a blazed grating in place of one of the interferometer mirrors to attain laser operation in the 9.3-μm band. The 10.6-μm laser was operated at a single longitudinal mode by injection locking an El-Op TEA laser with a low-pressure cw CO_2 laser with the configuration shown in Fig. 6.

IV. COMPUTER SIMULATION

The interaction between the electrons and the laser beams has been modeled and employed in a computer simulation to calculate the energy and phase trajectories of the electrons. The program numerically solves equations by a predictor-corrector numerical-integration technique. Electron trapping is demonstrated in the simulation by initiating the mean of a Gaussian electron energy distribution to be equal to the energy of resonance of the ponderomotive wave, and with a variance corresponding to the 3-eV (FWHM), measured energy spread. The initial electron distribution is uniform in phase space $\psi(0,t_0)$ (no prebunching of the beam), as illustrated in Fig. 7(a). The ordinate is the electron energy deviation with respect to energy of resonance (with the ponderomotive wave) $\delta\gamma=\gamma-\gamma_r$. The abcissa is the phase (ψ) of the electron relative to the ponderomotive wave. The separatrix of the ponderomotive potential (calculated with the experimental parameters) is indicated in the figure by a solid line. As the electrons propagate along the interaction region, the untrapped electrons are accelerated by the axial electric field. The electrons initially within the separatrix (trapped electrons), undergo synchrotron oscillations in closed orbits, and therefore remain inside the energy bounds of the separatrix and do not experience the acceleration of the axial field, as illustrated in Figs. 7(b) and 7(c). The energy distribution (the phase-space distribution integrated over all phases) and

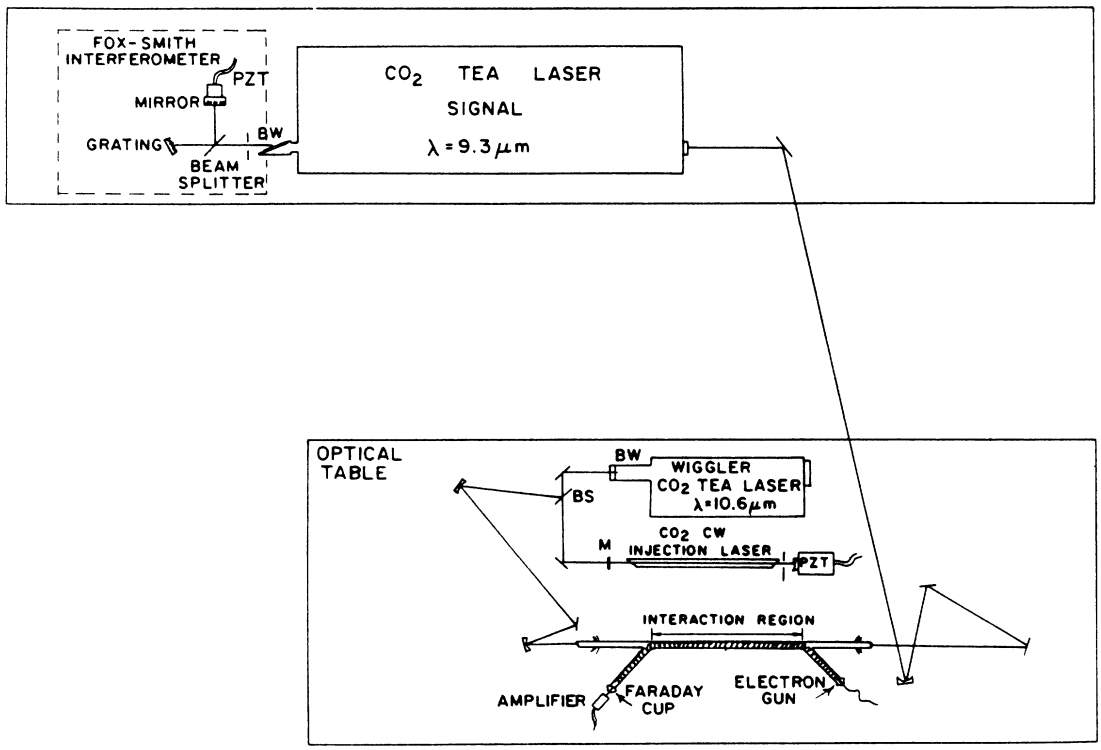

FIG. 6. Experiment schematic.

the average energy of the electron beam is depicted to the right. Also shown is the average energy of the beam if there were no radiation field present. The difference between these two energies ($\Delta\gamma$) corresponds to the energy transferred from the electron beam to the laser fields.

The phase-area displacement energy-transfer mechanism was simulated by reexecution of the simulation program with the mean energy of the electron beam initially less than (instead of equal to) the energy of resonance. This implies that the electrons enter the interaction region with a velocity less than the phase velocity of the ponderomotive wave. In the simulation, the distribution of the electrons was the same as in the trapping case, with the mean initially 5 eV below resonance. All of the electrons were accelerated through the energy of resonance, as illustrated in Figs. 8(a)–8(d). As expected, all of the electrons circumvented the phase-area domain of the separatrix. The average energies of the electron beam with and without the lasers present are again indicated on the right. In contrast to the trapping simulation, the average electron-beam energy with the lasers present is greater than the average without the lasers. The energy in which the electron beam was displaced is approximately equal to the area of the separatrix divided by 2π, as predicted by theory.[7] In this case, the electrons were accelerated at the expense of the lasers energy.

V. EXPERIMENTAL RESULTS

Initial experiments[13] were performed using a *decelerating* axial E field with the parameters of Table I and operated in the retarding potential mode (with the drift tube eliminated). The retarding electrode was set to $V_{\text{ret}} < 1$ V to reflect most of the electron current. The initial energy of the beam V_i was scanned to vary the position of synchronism along the interaction region. The signal intensity, which is proportional to the number of electrons acquiring energy from the radiation field, exhib-

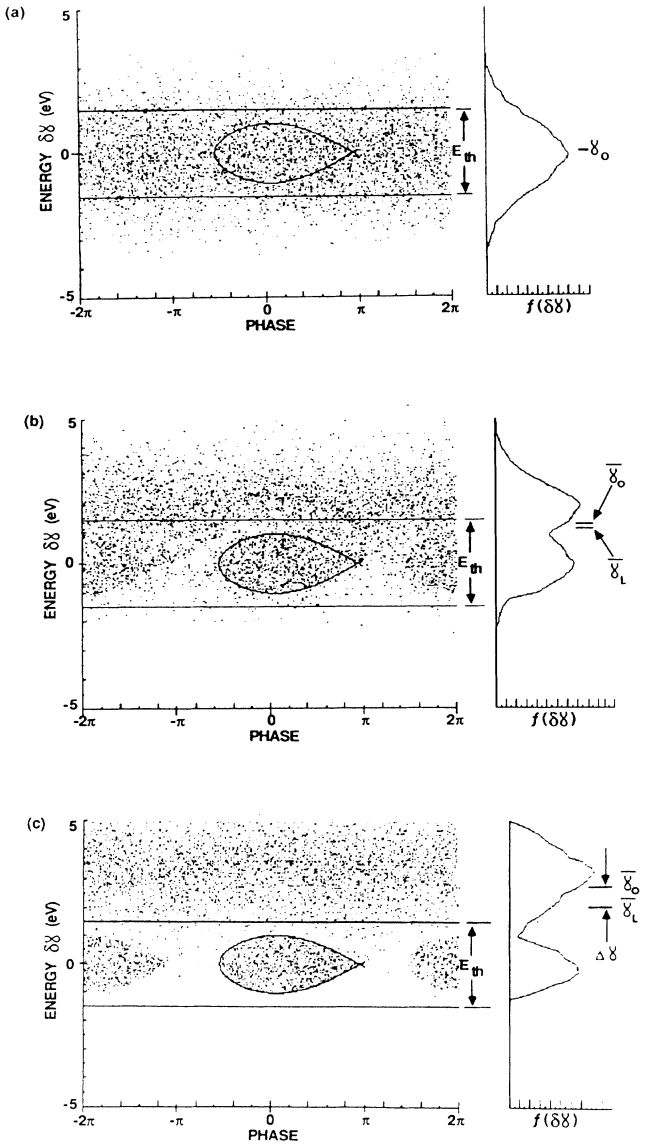

FIG. 7. Electron trapping simulation.

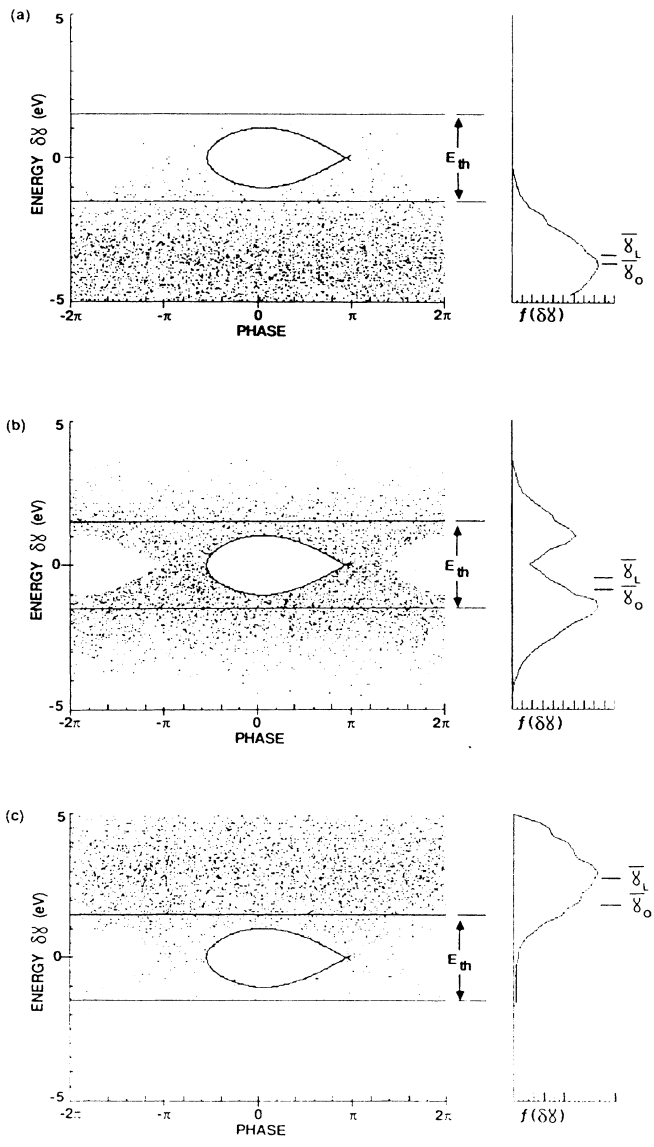

FIG. 8. Phase-area displacement simulation.

ited a resonance curve as a function of V_i as shown in Fig. 9. The peak of the curve corresponds to beam energy at synchronism condition with the beat wave in the center of the interaction region, where the laser fields were most intense. Its width corresponds to the potential drop along the interaction region ($E_{ac}L = 40$ V). These findings correspond well with the results expected for a PAD energy exchange at those characteristic resonance conditions. However, with this interpretation we explain the measured excess electron-current pulses as a result of PAD interaction-induced energy spread. The expected average *net* effect of PAD *deceleration* at these experimental conditions was supposedly less dominant and was not measured in this experimental phase.

The retarding-potential method does not give the electron energy spectrum in a single pulse. Scanning the energy during the pulse duration (150 nsec) is impractical, and therefore the measurement (Fig. 9) is only useful for determining a resonant transfer of energy to part of the electron beam, without indicating net acceleration. Moreover, the energy exchange in the interaction turned out to be smaller than the initial energy spread. It was hard, therefore, with the retarding-potential technique to resolve the direction of *net* energy transfer between the beam and the radiation field and distinguish between net average energy change and interaction-induced energy spread. In order to resolve this problem and distinctly identify the occurrence and conditions for trapped electron and PAD interaction effects, we revised the experimental setup to include a time-of-flight energy-analysis tube appended to the interaction region tube (see Fig. 4).

The second phase experiment (with the drift tube installed) was operated with essentially the same parameters of Table I but with $\lambda_s = 9.25$ μm, $\lambda_w = 10.59$ μm, $E_{ac} = 42$ V/m *(accelerating field)* and drift-tube voltage $V_{DT} = 10$ V. Figure 10 shows the measured collector current signal for two values of initial voltage of the beam: (a) $V_i = 1155$ V corresponding to synchronism near the center of the interaction region, and (b) $V_i = 1165$ V corresponding to synchronism precisely at the entrance to the interaction region. In both cases the signals appear with a transit time delay (~ 0.6 μS) relative to the coincident laser pulses, but the signals are temporally inverted relative to each other, indicating opposing energy-transfer directions. The oscilogram of Fig. 10(a) with an initially negative (excess current) signal followed by a positive (charge depletion) signal, indicates net electron acceleration by the laser pulses, as expected for a PAD energy exchange process. Conversely, the signal of Fig. 10(b) indicates electron deceleration and thus energy transfer to the radiation field in agreement with predictions for electron trapping.

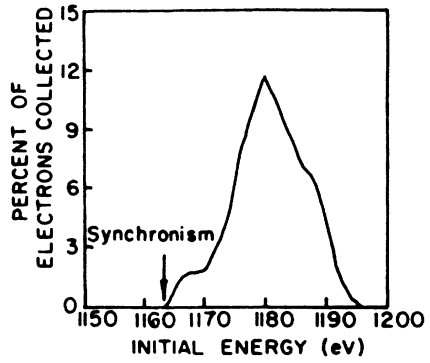

FIG. 9. Collector current signal vs initial electron energy. The arrow marks synchronism at the interaction region entrance.

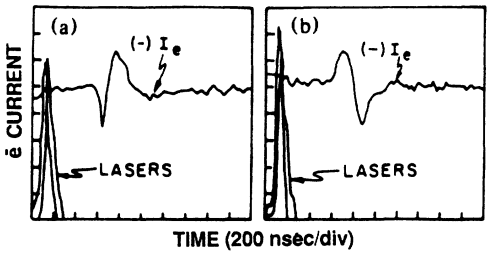

FIG. 10. Collector current signals corresponding to electrons (a) accelerated by the radiation field $V_i = 1165$ V trapping conditions, and (b) decelerated PAD conditions $V_i = 1155$ V.

VI. INTERPRETATION OF EXPERIMENTAL RESULTS

The dynamics of the electron propagation along the experimental tube under an accelerating dc field condition is depicted in Fig. 11. The diagrams in Figs. 11(a) and 11(b) display the kinetic energy of the electrons for the case of electron trapping and PAD interaction, respectively. The solid line corresponds to free-electron propagation in the absence of interaction with the radiation

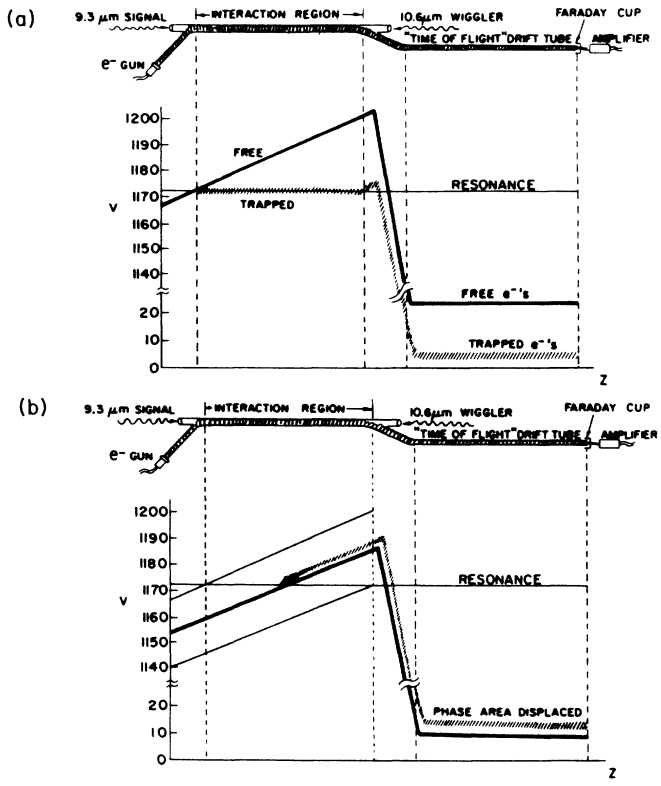

FIG. 11. Kinetic energy diagrams: (a) trapping, (b) PAD.

field, and the shaded lines correspond to interacting electrons. The axial electric field uniformly accelerates the free electrons throughout the interaction region at which point they are decelerated and drift at a low potential through the time-of-flight tube, as illustrated in Fig. 11(a). For an initial potential of 1165 V, the electrons become resonant with the ponderomotive potential at the start of the interaction region. At this point a portion of the electron beam gets trapped by the ponderomotive potential despite the accelerating field, and remain throughout the interaction length at a constant kinetic energy, about 1173 V, corresponding to the phase velocity of the ponderomotive wave.

Upon exit from the interaction region, all the electrons are decelerated by the same deceleration field. The untrapped electrons, for which the system is energy conserving, propagate thru the "time-of-flight" drift tube with a low kinetic energy equal to the drift-tube potential. The trapped electrons propagate in the drift tube with an energy lower by the amount lost in favor of the radiation field, which ideally is equal to the acceleration potential increment along the interaction region [Eq. (8)]. Consequently, in the time-of-flight energy-analysis experiment, the trapped electrons propagate in the drift tube appreciably slower than the untrapped ones. This results in a deficiency in the collected electron current signal with some delay after the lasers pulse, followed by an excess signal when the trapped electrons arrive.

When the initial beam energy is reduced such that the synchronism (resonance) with the ponderomotive wave is attained within the interaction region, as shown in the diagram of Fig. 11(b), PAD interaction conditions are attained. Hence the direction of net average energy exchange is reversed relative to the previous case. At the resonance point the electron beam attains excess acceleration by the radiation field. In a drift-tube energy-analysis experiment the electrons which are accelerated during the laser pulse duration, propagate faster in the drift tube. The collector would then detect an excess electron current pulse followed by a current deficient pulse, which is opposite of that expected for the electron-trapping mechanism.

In the first phase experiment, in which a retarding potential-energy-analysis method was used, the drift tube was not present, and the collector voltage was set to a low or negative value to diminish the collector current in the absence of the laser radiation field. The resonance curve of the collector current pulse shown in Fig. 9 was measured under conditions of a decelerating axial field. The resonance curve width is about equal to the decelerating potential drop along the interaction region, and the initial voltage range of the resonance curve corresponds well to attainment of synchronism (resonance) with the ponderomotive wave at points within the interaction region. This strongly suggests that the main effect measured in this experimental phase was a PAD interaction. However, it may be possible to interpret the hump in the region $V_i = 1165-1170$ V to result out of trapping effect, since it is close to the conditions of attaining synchronism right at the entrance to the interaction region (the initial voltage corresponding to this condition is marked with an arrow in Fig. 9). Because the retarding potential method did not enable measurement of net energy transfer to the beam, the measured resonance wave did not verify the theoretical predictions with regard to the direction of energy transfer between the electron beam and the radiation fields in the two interaction mechanisms. The measured excess current signals, clearly correlated with synchronism with the laser beat, can be attributed to net transfer of energy from the radiation field to the e beam as well as to energy spread effect induced by the interaction. Consequently the trapping and PAD interaction mechanisms were not separately identified.

As explained in the previous section, the second phase experiment, in which the time-of-flight energy-analysis technique was employed, enabled to separately identify and measure the energy exchange direction in the two different interaction mechanisms. The opposing polarity waveforms in Fig. 10 were measured at initial voltage conditions corresponding to PAD and trapping interactions, respectively, and indicate corresponding positive and negative energy transfer to the beam, as expected from the basic theory under the conditions of an accelerating axial field as with the experiment.

The excess current and defficient current signals are not resolved (spatially separated) in the recorded waveforms shown in Fig. 10. This indicates that the energy transfer between the e beam and the radiation field was smaller than the initial energy spread of the beam, contrary to the ideal case depicted in Fig. 11. It is therefore difficult to measure the quantity of energy transfer with the time-of-flight technique. A brief analysis of the current pulse propagation in the drift tube will help to clarify this point and derive some more quantitative conclusions from the measured current waveforms.

The instantaneous current $I(z,t)$ at any coordinate z along the drift tube is given by

$$I(z,t) = -e \int v_z f_{v_z}(v_z,z,t) dv_z \ , \tag{10}$$

where f_{v_z} is the axial velocity distribution function of the electron beam in the tube, and is expressible in terms of the longitudinal energy distribution function using the relation

$$f_{v_z}(v_z,z,t) = f_E(v_z,z,t)\frac{dE}{dv_z} = m v_z f_e(E,z,t) \ . \tag{11}$$

The velocity distribution function which solves the forcefree Vlasov equation in the drift tube has the general form

$$f_{v_z}(v_z,z,t) = f\left[v_z, 0, t - \frac{z}{v_z}\right] \ , \tag{12}$$

where $z = 0$ is the entrance point to the drift tube.

We model the interaction process by assuming an instantaneous impulse shift in the velocity distribution of a fraction $K < 1$ of the electrons in the beam, occurring at time t_0 which is coincident with the narrow laser pulse duration

$$f(v_z,0,t)=[1-K\delta(t-t_0)]f^0_{v_z}(v_z) + Kf^a_{v_z}(v_z)\delta(t-t_0)\ , \tag{13}$$

where $f^0_{v_z}$ is the initial axial velocity distribution (in the absence of a radiation field), and $f^a_{v_z}(v_z)$ is the axial velocity distribution function of the perturbed (radiatively interacting) electrons. We further assume that the interaction effect can be modeled by merely a shift ΔE in the energy distribution of the noninteracting electrons $f^a_E(E)\sim f^0_E(E-\phi E)$. By substituting this into Eqs. (8)–(11), we obtain after executing the integration over axial velocities $I=I_0+\Delta I(z,t)$, where I_0 is the unperturbed current and $\Delta I(z,t)$ is the time-dependent current signal in the region $z>0$:

$$\Delta I(z,t)\propto K\frac{E(v_z)}{t-t_0}[f^0_E(E(v_z))-f^0_E(E(v_z) -\Delta E)]\Big|_{v_z=z/(t-t_0)}\ . \tag{14}$$

If the energy spread of the distribution function $E_{\rm th}$ is much larger than the energy acceleration ΔE of the interacting electrons $-E_{\rm th}\gg\Delta E$, then Eq. (12) can be simplified to

$$\Delta I(z,t)=\frac{K\Delta E}{t-t_0}E(v_z)f^{0'}_E E(v_z)\Big|_{v_z=z/(t-t_0)}\ . \tag{15}$$

For a normal single-peak distribution function f^0_E (e.g., a shifted Gaussian) the current signal function (14) describes two counterpolarity current pulses, which, for a fixed z coordinate (collector position), are delayed in time relative to each other and relative to the generating impulse time t_0. In the limit $E_{\rm th}\gg\Delta E$ the two pulses are not resolved in time and would form an s-shaped signal described by Eq. (15). The longer the drift distance z is, the longer the delay time, but the signals tend to spread out becoming wider and smaller in amplitude. It is evident from Eqs. (14) and (15) that the order of the positive and negative current pulses in time (whether resolved or not) depends on the sign of the energy transfer ΔE, so that acceleration and deceleration can be distinguished by the shape of the signal. However, quantitative measurement of the energy transfer ΔE is only possible in the limit $E_{\rm th}\ll\Delta E$ [Eq. (14)], where it is deductible from the delay time of the pulses. In the opposite limit [Eq. (15)], the ΔE appears only as a coefficient, determining the amplitude of the current signal, but since it also multiplies the unknown parameter K, measurement of the current signal amplitude does not provide an estimate of ΔE.

The measured current signal traces shown in Figs. 10(a) and 10(b) have the typical s-shaped form as expected from the current signal expression (15) with a normal single-peaked distribution function $f^0_E(E)$. In Fig. 10(a), a current excess pulse followed by a current deficiency pulse corresponds distinctly to transfer of energy from the radiation field to the electron beam, as expected theoretically for a PAD interaction process under conditions of an accelerating axial electric field and synchronization within the interaction region [Fig. 11(b)]. The opposite polarity waveform of Fig. 10(b) corresponds to negative transfer of energy as expected theoretically for a trapping interaction process under conditions of an accelerating field and synchronization at the entrance to the interaction region.

A close examination of the waveforms in Figs. 10(a) and 10(b) reveals that the two signals differ not only by polarity, but also by delay time. While the zero crossing of the waveform in Fig. 10(a) is delayed about 550 nsec relative to the peak of the laser pulses, this delay is about 650 nsec in Fig. 10(b). This agrees with the expectations for a case $E_{\rm th}>\Delta E$ for which Eq. (14) rather than Eq. (15) should be used to describe the waveform, and the energy exchange parameter may be roughly estimated from the signal waveform despite the partial overlap of the positive and negative pulses.

In order to determine the approximate amount of energy exchanged, a simulation of the electron transport dynamics in the time-of-flight (TOF) tube was performed. The simulation made use of the known initial electron energy distribution, which was measured (prior to laser firing) by measuring the collector current while scanning the potential of the retarding electrode in front of the collector. The measured data points are depicted in Fig. 12(a) by heavy dots, and fit well to a model Gaussian distribution function with standard deviation of 1.6 eV and center *longitudinal* energy of 7 eV (though the drift-tube voltage and therefore the *total* beam kinetic energy was 10 V). Also shown in Fig. 12(a) is the longitudinal energy distribution of the perturbed electrons, assuming an energy loss of 2 eV during the interaction with the lasers.

Figure 12(b) shows the simulated unperturbed (current deficient) pulse and the perturbed (current excess) pulse as they appear as a function of time at the end of the drift tube. These pulses correspond, respectively, to the first and second terms of Eq. (12) with $\Delta E=-2$ eV. The difference between the pulses represents the net collector current signal [Eq. (14)]. In order to evaluate the delay times, the laser pulse (represented as an impulse) is marked t_0 at the bottom of the diagram.

The same simulation program was also applied to tracing the current signal development in the drift tube under the same initial conditions for the unperturbed electrons and an energy distribution shifted by $\Delta E=1.5$ eV modeling the perturbed electron distribution [see Fig. 13(a)]. The results of this simulation are shown in Fig. 13(b) depicting an inverted waveform [relative to the one in Fig. 12(b)] with a slightly shorter delay time.

The similarity in shape, polarity, and delay time between the simulated current signal waveforms of Figs. 13(b) and 12(b) and the corresponding measured oscillogram traces shown in Figs. 10(a) and 10(b), supports our interpretation of corresponding positive and negative energy transfer by respective PAD and trapping mechanisms in the two cases. It also allows us to estimate the quantity of energy exchanges in the experiment to be about $\Delta E=1.5$ eV in the first case (PAD) and $\Delta E=-2$ eV in the second case (trapping), based on the similarity with the model calculation which results with the same parameters.

The amount of energy exchanges expected theoretically

in the PAD interaction mechanism was calculated using Eq. (9) and the experimental parameter values, which were close to the ones given in Table I. The result $\Delta E = 1.5$ eV compares well with the estimate based on the measured current signal and its simulation. On the other hand, the calculated energy exchange by the trapping effect deviates substantially from the estimated value of $\Delta E = -1.6$ eV deduced from the experimental waveform trace and the simulation program. In the second phase experiment an accelerating field of $E_{ac} = 42$ V/m was applied along the 0.6-m-long interaction region. According to Eq. (8) the trapped electrons should have lost 25 eV in favor of the radiation field if they remained trapped throughout the entire interaction region. The fact that the energy transferred with the electron trapping mechanism was only $\simeq 2$ eV for electron trapping implies that the electrons must have become detrapped after 5 cm. This was possibly due to nonuniformities in the dc fields, lateral deviations in the overlapping of the beams, or the finite coherence of the laser beams.

The experimental data demonstrates that both trapping and PAD mechanisms of energy exchange were observed in the stimulated Compton-scattering scheme at the conditions predicted by theory. Due to the large initial beam energy spread, which was apparently larger than the net energy transfer, the positive and negative parts of the signals were not completely resolved in time, and it was hard to determine the exact amount of energy exchanged with the radiation field in either mechanism. However, simulation of the drift-tube transport dynamics with the known initial electron energy distribution (measured by scanning the retarding potential) and with assumptions of energy transfer $\Delta\bar{E} \simeq +1.5$ eV and $\Delta\bar{E} \simeq -2.0$ eV, fitted reasonably well with the waveforms of Figs. 10(a) and 10(b), respectively. The $+1.5$-eV PAD energy transfer compares well with the $\bar{E} \simeq +1.6$ eV predicted from Eq. (9). The -2.0-eV energy transfer corresponds to electron detrapping after 5 cm, possibly due to nonuniformities in the dc fields, lateral deviations in the overlapping of the beams, or the finite coherence of the laser beams.

The successful demonstration of energy exchange by nonlinear regime Compton scattering in the present experiment makes way for further fundamental interaction

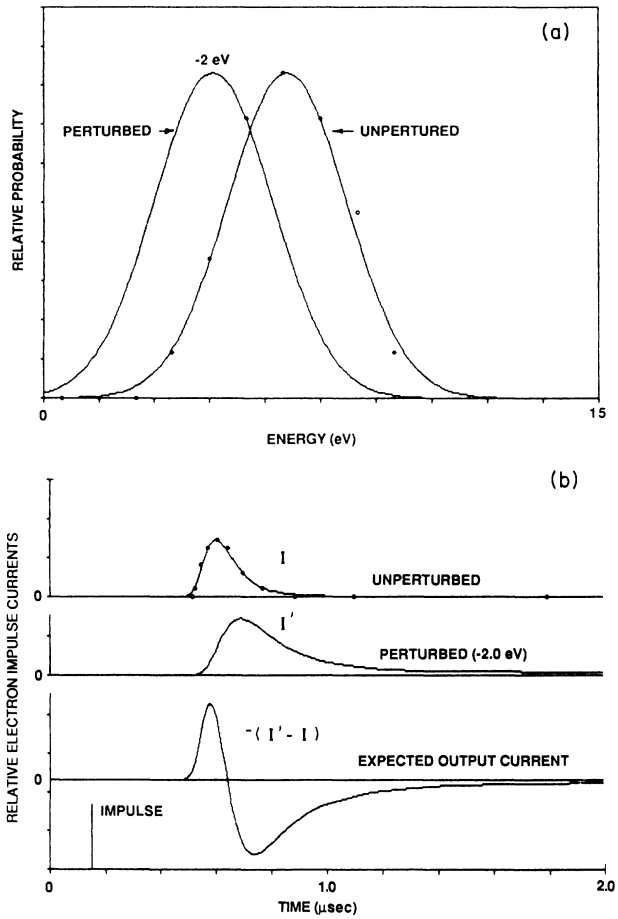

FIG. 12. (a) Electron energy distributions before and after trapping interaction. (b) Drift-tube electron impulse response—electron trapping. Measured e^- temporal energy distribution (upper). Simulated perturbed e^- temporal energy distribution (middle). Simulated e^- output current (lower).

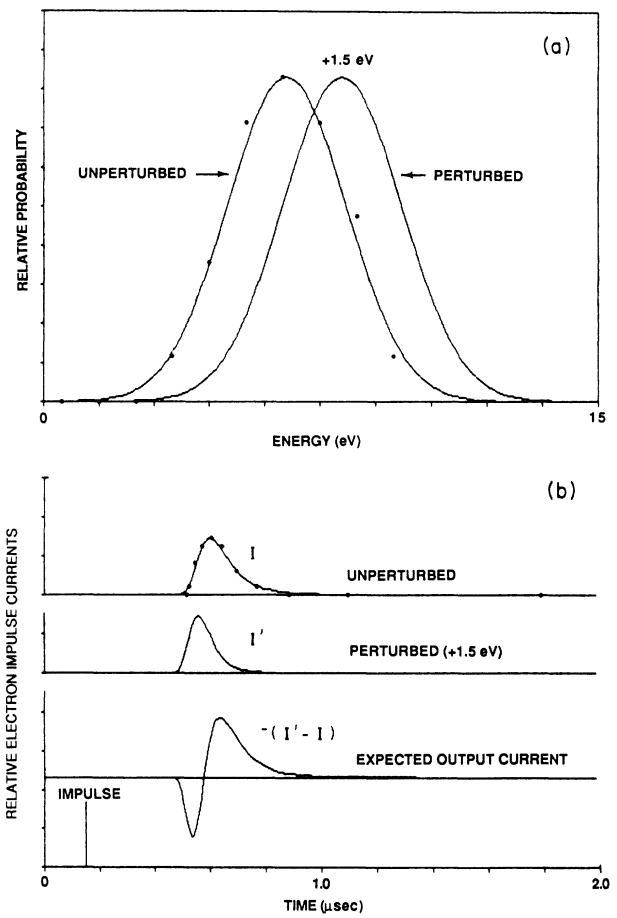

FIG. 13. (a) Electron energy distributions before and after PAD interaction. (b) Drift-tube electron impulse response—PAD. Measured e^- temporal energy distribution (upper). Simulated perturbed e^- temporal energy distribution (middle). Simulated e^- output current (lower).

and FEL related studies in a small-scale laboratory system. Further experiments to be carried out with this system will provide opportunities to study important interaction aspects of phase-area displacement and trapping mechanisms; for example, effects of nonadiabatic changes in the interaction parameters and incoherence of the wiggler and signal waves. The large number of wiggler periods (5×10^4) and trap synchrotron oscillations (~40) puts this laser-beat experiment in the interesting regime of very long wiggler FEL's and laser accelerators, where studies of phase-space evolution have important fundamental and applied research implications.

While the parameters of the experimental system used to attain the presently reported results enable basic study of electron–laser-beat interaction effects, they certainly are not appropriate for demonstrating a useful FEL device. We note, however, that CO_2 lasers with powers at least five orders of magnitude higher than the ones used by us are available in research laboratories. With an appropriate relativistic electron beam to provide a substantial Doppler-shifted frequency up conversion, such schemes may be considered for efficiency enhanced em pump FEL schemes as suggested and analyzed in Ref. 2.

ACKNOWLEDGMENTS

This work was supported initially by U.S. Air Force (USAF) Grant No. AFOSR 82-0239 and subsequently by endowments from the Kranzberg Institute and Israeli Universities funding committee. I. Katz, A. Eichenbaum, I. Burak, B. Cohen, P. Yogev, and B. Lissak made important contributions to the experiment construction.

[1]R. Z. Olshan, A. Gover, S. Ruschin, and H. Kleinman, Phys. Rev. Lett. **58**, 483 (1987).

[2]P. L. Kapitza and P. A. M. Dirac, Proc. Cambridge Philos. Soc. **29**, 197 (1933).

[3]M. V. Fedorov, Prog. Quantum Electron. **7**, 73 (1981).

[4]R. H. Pantell, G. Soncini, and H. E. Puthoff, IEEE J. Quantum Electron **QE-4**, 905 (1968).

[5]D. A. G. Deacon *et al.*, Phys. Rev. Lett. **38**, 892 (1977).

[6]E. D. Courant, C. Pellegrini, and W. Zakowicz, Phys. Rev. A **32**, 2813 (1985).

[7]N. M. Kroll, P. Morton, and M. N. Rosenbluth, IEEE J. Quantum Electron. **QE-17**, 1436 (1981).

[8]M.N. Rosenbluth, B. N. Moore, and H. V. Wong, IEEE J. Quantum Electron. **QE-21**, 1026 (1985).

[9]A. Gover, C. M. Tang, and P. Sprangle, J. Appl. Phys. **53**, 124 (1982).

[10]C. A. Brau, IEEE J. Quantum Electron. **QE-21**, 824 (1985); T. J. Orzechowski *et al.*, *ibid.* **QE-21**, 831 (1985).

[11]L. S. Bartell, H. Bradford, and R. R. Roskov, Phys. Rev. Lett. **14**, 851 (1965).

[12]R. Z. Olshan, Ph.D. Dissertation, Tel-Aviv University, Israel, 1987.

[13]R. Z. Olshan *et al.*, Nucl. Instrum. Methods Phys. Res. **A250**, 253 (1986).

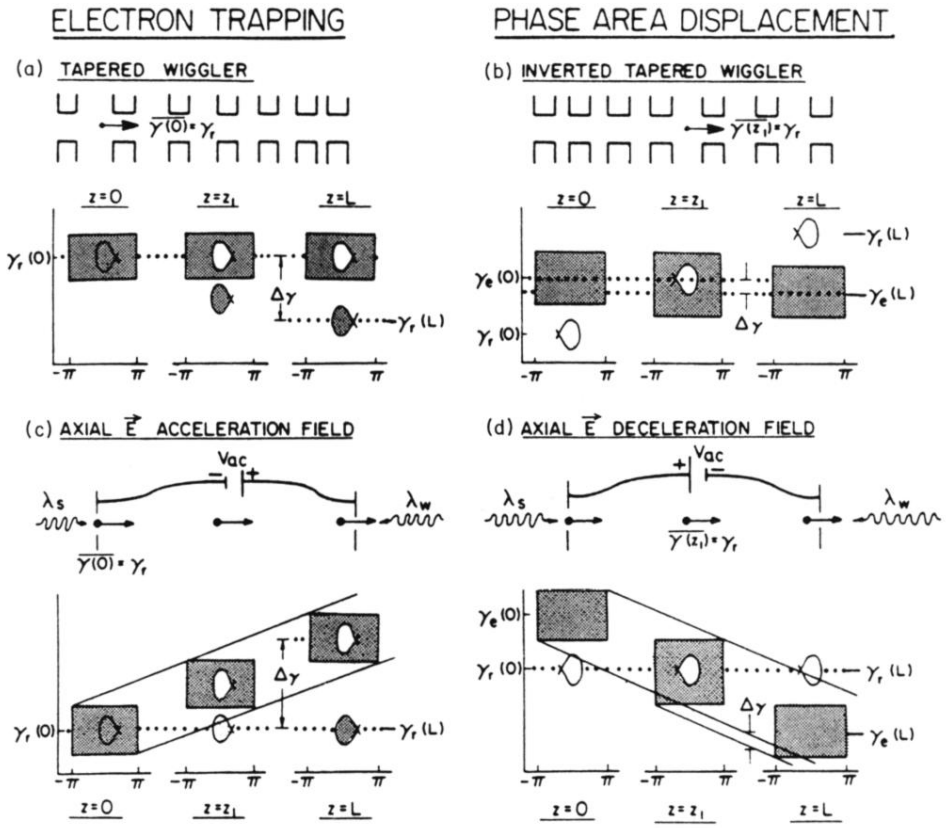

FIG. 1. Phase-space diagrams for electron energy extraction: (a) and (c) electron trapping; (b) and (d) phase-area displacement.

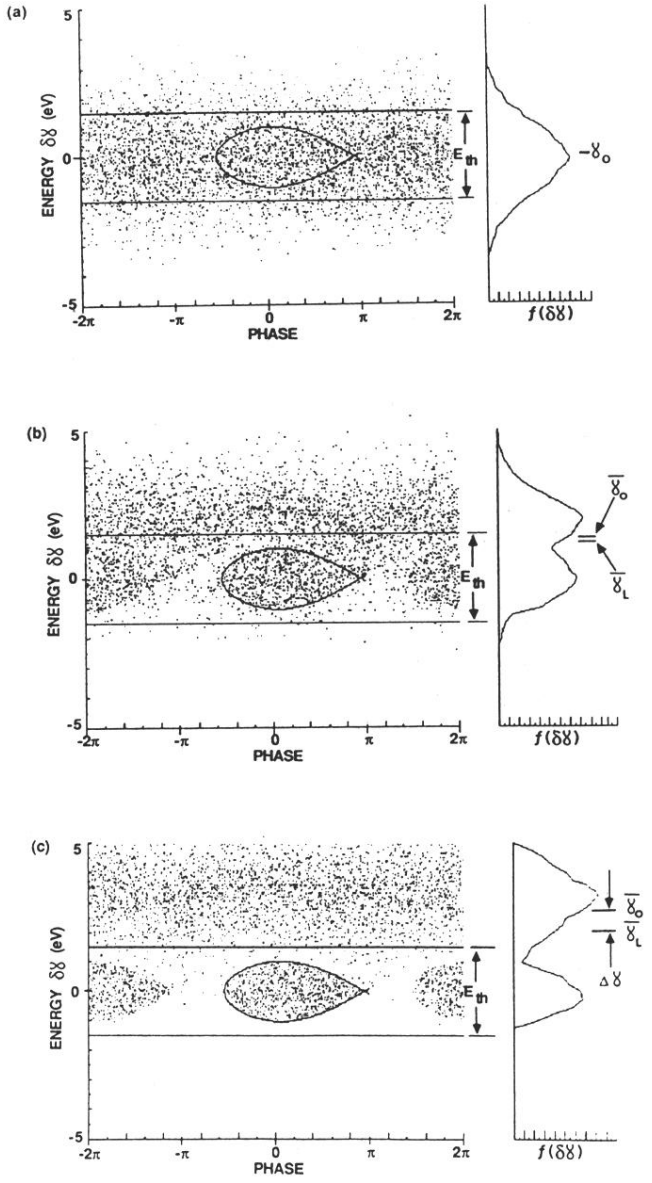

FIG. 7. Electron trapping simulation.

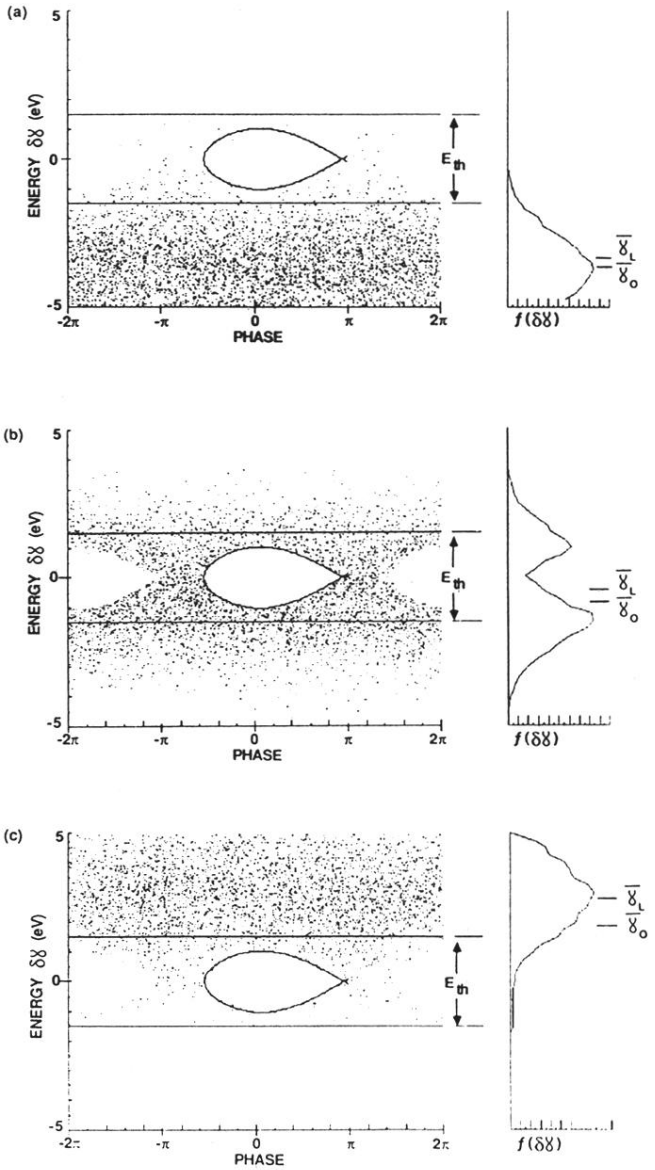

FIG. 8. Phase-area displacement simulation.